



Potential benefit of extra radiosonde observations around the Chukchi Sea for the Alaskan short-range weather forecast

Min-Hee Lee^a, Joo-Hong Kim^{a,*}, Hyo-Jong Song^b, Jun Inoue^c, Kazutoshi Sato^d, Akira Yamazaki^e

^a Korea Polar Research Institute, Incheon, South Korea

^b Korea Institute of Atmospheric Prediction Systems, Seoul, South Korea

^c National Institute of Polar Research, Tachikawa, Japan

^d Kitami Institute of Technology, Kitami, Japan

^e Japan Agency for Marine-Earth Science and Technology, Yokohama, Japan

ARTICLE INFO

Keywords:

Arctic ocean
Weather forecasts
Ship-borne radiosonde observation
Data assimilation
Observing system experiment

ABSTRACT

In recent years, growing attentions have been paid to the potential benefit of extra observations over the data-sparse Arctic Ocean for weather forecasts. Here we also focus on such a case by targeting the inhabited land area, Alaska. During 2–18 August 2015, ship-borne radiosonde sounding observations were performed every 12 h (except 6-hourly from 12:00 UTC 11 August to 00:00 UTC 14 August) around the Chukchi Sea. To assess the impact of those extra radiosonde observations, two sets of ensemble forecast experiments (CTL_f and OSE_{A_f}) were produced, which were respectively initialized by atmospheric reanalysis data without (CTL) and with (OSE_A) additional assimilation of those data. The tropospheric circulation fields are compared to verify their differences in forecast performance. While two forecasts have similar performance in the earlier spin-up period of the analysis-forecast cycle (from 4 to 7 August), their performance tends to diverge in the later period (from 11 to 18 August) due to the accumulated influence on the error reduction in OSE_{A_f}. Among the improved forecasts in OSE_{A_f}, two most outperformed forecasts, each initialized on 00:00 UTC 12 and 00:00 UTC 14, show a notable improvement in predicting the developing trough over Alaska on 16–17 August by suppressing the development of erroneous high anomalies in CTL_f. Though the positive impact of single-point observations is limited in a space, our results suggest that enhanced radiosonde profile observations in the data-sparse polar ocean could be beneficial for the forecasts beyond the observational area.

1. Introduction

The Arctic receives considerable attention from both the public and science community under recent rapid climate change. Beyond its passive role as an energy sink of the globe, the accelerating Arctic warming in recent decades made the Arctic more active in forming its nonlinear interaction with the adjacent regions (Overland et al., 2016). For example, the Arctic warming under climate change and associated weakening of the polar vortex is now a usual suspect of the severer winter cold extremes in the NH (refer to Table 1 for all abbreviations hereafter) mid-latitudes (Cohen et al., 2014; Kim et al., 2014; Mori et al., 2014; Overland et al., 2016). In addition to the cold season, the warm season changes in NH mid-latitude atmospheric circulation affecting heat waves have been also detected in the past observations in a consistent manner with climate models, which is also attributed to the rapid Arctic warming (Coumou et al., 2015).

Given the emerging role of the Arctic in NH weather and climate, a

lack of a sustainable observing network in the Arctic is a big issue, which could be the substantial source of uncertainties in weather and climate forecasts, limiting prediction ability in the NH mid-latitudes. The ongoing international effort, such as the ‘YOOP’ for the period 2017–19, would extensively evaluate the predictability source from the Arctic (Jung et al., 2016). Prior to the YOOP period, however, several studies have already shown the positive impact of extra Arctic observations on the wider range weather and sea ice prediction using of numerical models (Inoue et al., 2015; Ono et al., 2016; Sato et al., 2017; Yamazaki et al., 2015). The extra Arctic observations with great interest were the radiosonde vertical atmospheric profiles over the data-sparse Arctic Ocean obtained by R/Vs, such as the Korean *Araon*, Japanese *Mirai*, German *Polarstern*, Norwegian *Lance*, etc. In the previous studies, OSEs were carried out with and without the extra radiosonde profiles, by which the impact of the extra data on the forecast performance of extreme weather events or sea ice distribution was evaluated.

The Korean ice-breaking R/V *Araon* has regularly cruised the Pacific

* Corresponding author. Korea Polar Research Institute, 26 Songdomirae-ro, Yeonsu-gu, Incheon, 21990, South Korea.

E-mail address: joo-hong.kim@kopri.re.kr (J.-H. Kim).

<https://doi.org/10.1016/j.polar.2018.12.005>

Received 12 June 2018; Received in revised form 30 November 2018; Accepted 11 December 2018

Available online 11 December 2018

1873-9652/ © 2018 Elsevier B.V. and NIPR. All rights reserved.

Table 1
Description of all abbreviations used in this study. The abbreviations are presented sequentially in order of their first appearance in the text.

Abbreviation	Description
NH	Norther Hemisphere
YOPP	Year of Polar Prediction
R/V	Research vessel
OSE	Observing system experiment
ALEDAS2	The second-generation JAMSTEC global ensemble data assimilation system
JAMSTEC	Japan Agency for Marine Earth Science and Technology
AFES	The atmospheric general circulation model for the Earth Simulator
LETKF	Four dimensional local ensemble transform Kalman filter
GTS	Global telecommunication system
NCEP	National Centers for Environmental Prediction
NOAA	National Oceanic and Atmospheric Administration
OISST_V2	Optimum interpolated sea surface temperature version 2
ECMWF	European Center for Medium-Range Weather Forecasts
ERA-I	ECMWF's interim reanalysis
ALERA2	The second-generation ensemble reanalysis data from AFES with ALEDAS2
CTL	Conventional ALERA2 ensemble reanalysis data
OSE_A	ALERA2 with the assimilation of extra radiosonde observations on the Araon
CTL _f	Forecast experiments with the initial conditions of CTL
OSE_A _f	Forecast experiments with the initial conditions of OSE_A
H500	Geopotential height at 500 hPa
AE	Absolute error (i.e., analysis or forecast fields minus ERA-I)
RMSD	Root mean square distance
F12	Forecast experiments with the initial condition at 00:00 UTC 12 August
T500	Air temperature at 500 hPa
PT850	Potential temperature at 850 hPa
MSLP	Mean sea level pressure
F14	Forecast experiments with the initial condition at 00:00 UTC 14 August
PV	Potential vorticity
IAU	Incremental analysis updating

Arctic sector during August and early September since 2010. Since 2015, the radiosonde atmospheric profiles have been obtained on the vessel over the data-sparse Arctic seas. In 2015, twice-daily observations were first conducted every 00:00 and 12:00 UTC from 4 August to 18 August, except four times a day from 12:00 UTC 11 August to 00:00 UTC 14 August. Those radiosonde data from the Korean R/V were first applied to a global ensemble data assimilation system called ALEDAS2 developed at the JAMSTEC, which is composed of the AFES (Ohfuchi et al., 2004) and the four-dimensional LETKF (Enomoto et al., 2013; Miyoshi and Yamane, 2014). Two sets of ensemble forecast experiments produced by the ALEDAS2 (i.e., one without and the other with the additional assimilation of the Araon radiosonde data) are compared to investigate the impact of the extra observations. In the present study, we mainly focus on the forecast performance over Alaska, because this region is the nearest downstream-side inhabited land area from the observational area. Our study would augment the existing opinion about the usefulness of the extra observations over the data-sparse Arctic Ocean.

Section 2 provides the information of observation data and the description of the forecast experiments. Section 3 shows the improved performance in the forecasts of the Alaska province with the additional radiosonde data assimilation and seeks the dynamical origin of the improvement. Finally, summary and discussion are presented in Section 4.

2. Observations and forecast experiments

2.1. Observation data

The 2015 Araon summer Arctic expedition leg 1 began on 1 August at Nome and ended on 22 August at Barrow. The radiosonde had launched mostly twice a day from 00:00 UTC 2 August to 12:00 UTC 18 August, except four times a day from 12:00 UTC 11 August to 00:00 UTC 14 August. The entire cruise track and the radiosonde observational points are shown in Fig. 2a. The data were not broadcasted through the GTS, which means that routine weather forecasts did not use them. The radiosonde observations provide us the vertical profiles

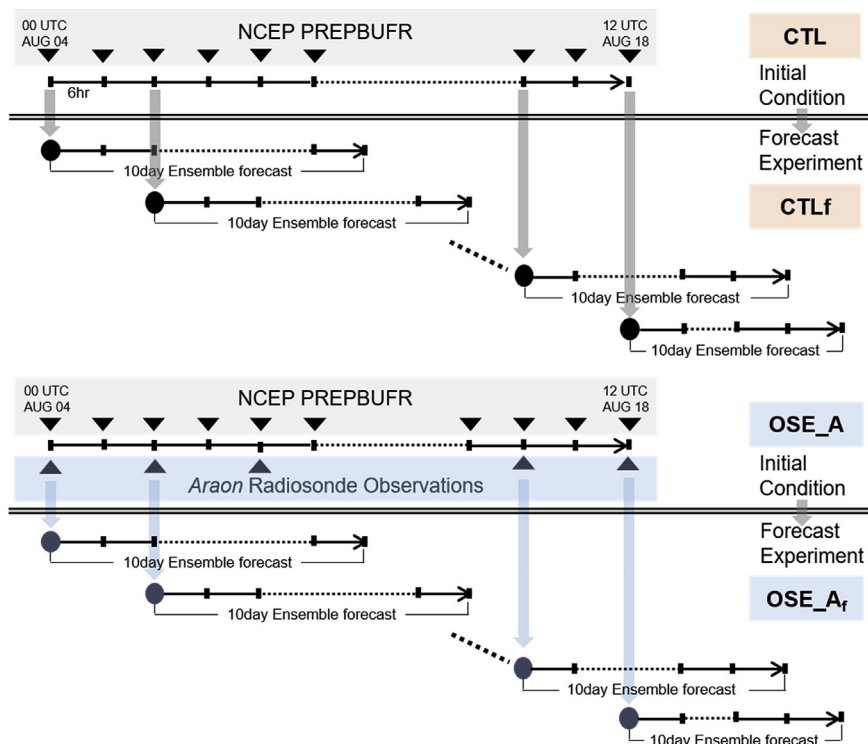


Fig. 1. Schematic processes to produce the ensemble reanalysis (ALERA2) and forecast using the ALEDAS2. CTL is the original ALERA2 ensemble reanalysis with the assimilation of the 6-hourly NCEP PREPBUFR data (inverted triangles); CTL_f is the ALEDAS2 ensemble forecast initialized by the CTL reanalysis; OSE_A is the same as CTL, except with the addition of extra radiosonde observations on the R/V Araon (triangles); OSE_A_f is the same as CTL_f, except initialized by the OSE_A reanalysis.

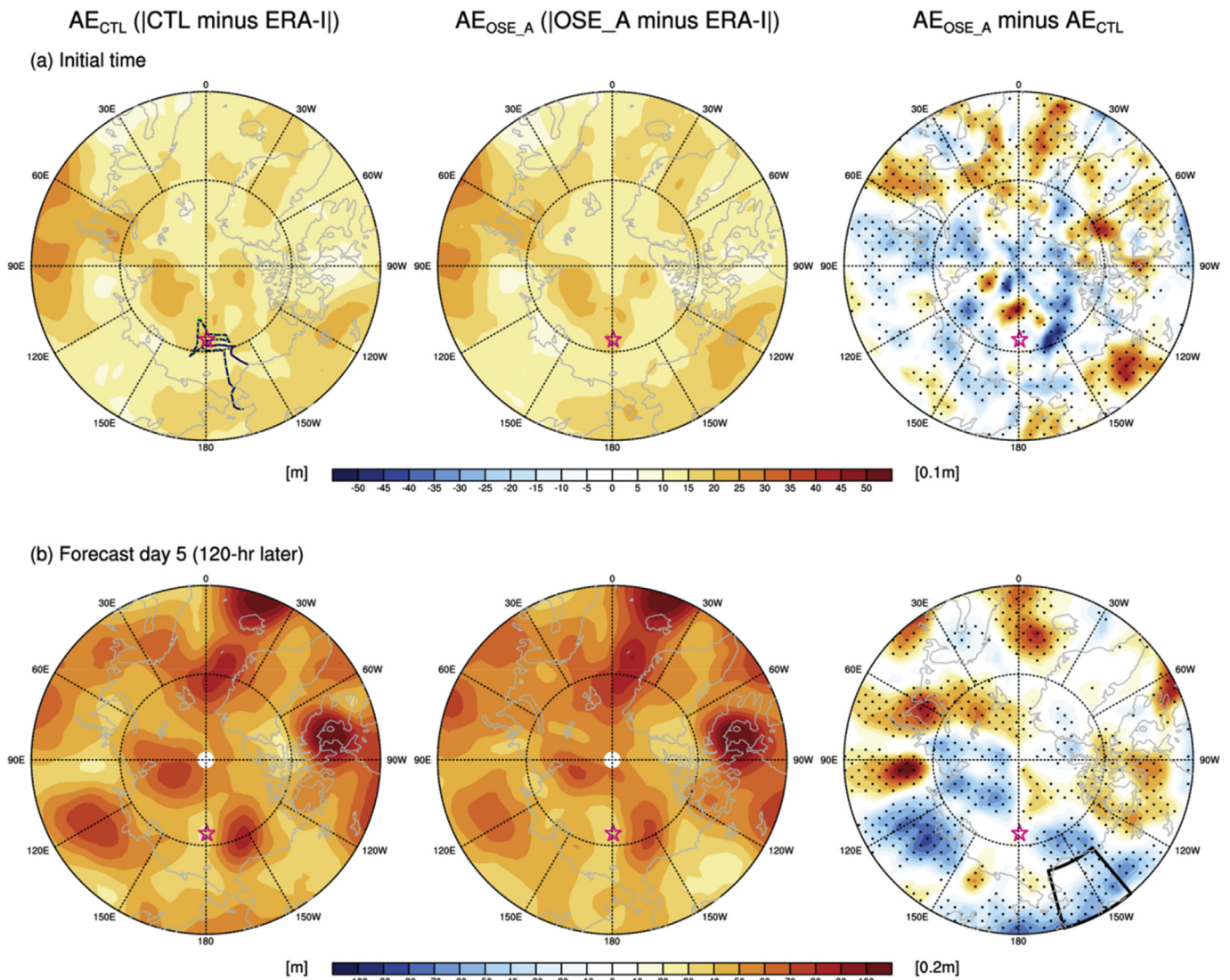


Fig. 2. The average AEs of H500 for both CTL_f (left column, AE_{CTL}) and OSE_A_f (middle column, AE_{OSE_A}) (a) at the initial time and (b) 5-day (120-hr) later in comparison with the ERA-I, as well as their differences (right column; i.e., AE_{OSE_A} minus AE_{CTL}). Here the CTL and OSE_A reanalysis data are used at the initial time. The cruise track of the R/V *Araon* is overlaid in (a) and the average position is marked with a red star symbol. In the rightmost panels, the dots represent the statistically significant grid points ($p < 0.05$) based on bootstrap resampling and the box denotes the Alaska domain. The difference plots use the color bar with scaled units (multiplied by 0.2). (For interpretation of the references to color in this figure legend, the reader is referred to the Web version of this article.)

of air temperature, relative humidity, and horizontal wind direction and speed up to the lower stratosphere. Air temperature data show an appreciable shift to the Arctic regime (i.e., lowered tropopause) at 12:00 UTC on 4 August when the ship passed 72°N (figure not shown).

The 6-hourly NCEP PREPBUFR dataset is used as the source of global observations. The global observation dataset is basically necessary to produce the atmospheric reanalysis fields used as the initial conditions of forecasts. The NOAA 0.25° daily OISST.v2 is used as the ocean and ice surface boundary conditions. As a reference dataset, the 6-hourly ECMWF's ERA-I is used (Dee et al., 2011).

2.2. Forecast experiments

An ensemble reanalysis version 2 using the ALEDAS2 produces the ALERA2 dataset with the assimilation of the 6-hourly NCEP PREPBUFR global observation data. In the analysis cycle of the ALEDAS2 ensemble forecast (63 members), the ALERA2 data are produced at temporal, horizontal and vertical resolutions of 6-h, T119 (about 1°) and L48 (sigma level up to 3 hPa), respectively. In addition, another experimental ensemble reanalysis dataset is generated by the OSE with the

additional assimilation of all the *Araon* radiosonde observations. Hereafter the former original ALERA2 dataset is called CTL and the latter experimental reanalysis dataset is called OSE_A.

To investigate the impact of the extra radiosonde observations on the ALEDAS2 forecast, we perform two sets of the 63-member ensemble forecast experiments using the same lower boundary conditions of the NOAA OISST.v2 ocean and sea ice, but with different initial conditions of two reanalysis datasets (i.e., CTL vs. OSE_A). Here two forecast experiment sets are respectively referred to as CTL_f and OSE_A_f. Due to the use of those observed lower boundary conditions, our forecast experiments are not 'real' forecasts, but literally 'experimental' forecasts. However, the results are potentially useful to assess the impact of improved initial conditions by assimilating extra radiosonde observations over the data-sparse Arctic Ocean, which meets the purpose of this study. The 10-day ensemble forecast integrations were performed with the initial time at 12-h intervals from 00:00 UTC 4 August to 12:00 UTC 18 August. Thus, both CTL_f and OSE_A_f consist of 30 forecast experiments (i.e., twice a day for 15 days). The producing processes of the two sets of reanalyses and forecast data are schematically presented in Fig. 1.

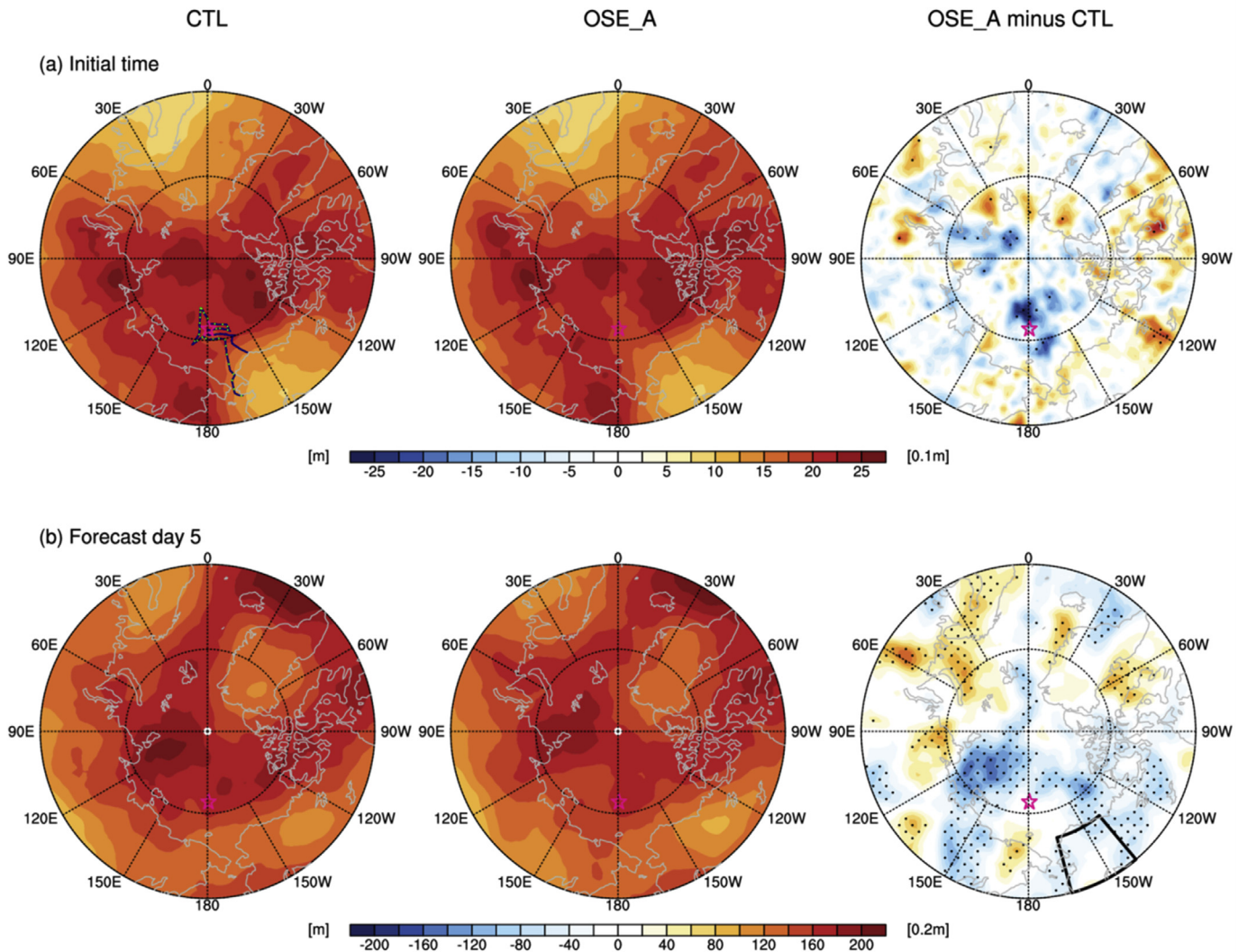


Fig. 3. Same as Fig. 2, except for the average ensemble “spreads” (or uncertainty) of CTL_f and OSE_{Af}.

3. Results

3.1. General assessment of the impact of additional assimilation

Averaged performances of the reanalysis and the 5-day forecast are compared based on the H500, which is the typical skill indicator of operational forecast models. For comparison, ERA-I are also employed as the reference reanalysis. Fig. 2 shows the average (i.e., averaged for 30 initial conditions, each containing 63 ensemble members) AEs of CTL_f and OSE_{Af}, (both at the initial time and 5-day after) in comparison with ERA-I (i.e., $AE_{CTL} = |CTL_f \text{ minus ERA-I}|$, $AE_{OSE_A} = |OSE_{Af} \text{ minus ERA-I}|$), as well as their differences (i.e., $AE_{OSE_A} \text{ minus } AE_{CTL}$). For the differences of the average AEs between OSE_{Af} and CTL_f, the statistical significance ($p < 0.05$) is tested by using the bootstrapping method (Hesterberg et al., 2003) with bootstrapped 10,000 random samples. In addition, the average (i.e., averaged for 30 initial conditions) ensemble spreads are contrasted between CTL_f and OSE_{Af} to measure the magnitude of the forecast error (Fig. 3). Here the ensemble “spread” (or uncertainty) is defined by the difference of two ensemble members each having the maximum and minimum values at a grid point.

The individual gross patterns of both AEs and ensemble spreads have a similarity between CTL_f and OSE_{Af} (left panels vs. middle panels), because they are primarily determined by an inherent

performance of the forecast system. However, the pattern of difference reflects the impact of different observational input to the forecast system. At the initial time, the reduced AEs in OSE_A are distributed in the Arctic Ocean and the northern Russia–western Alaska sector between 60°E to 150°W, while, in rest regions, larger AEs appear in OSE_A (the right panel of Fig. 2a). The 5-day forecast also show coexistence of both reduced and increased errors in the field of difference (the right panel of Fig. 2b). Compared with the initial time, the error pattern appears to rotate eastward. As a result, the reduced AEs in OSE_{Af} are appreciable over the eastern Arctic Ocean, central Siberia, the Bering and Beaufort seas, and Alaska. Concerning the ensemble spread, the larger reduction in OSE_A is found around the observational locations at the initial time (the right panel of Fig. 3a), while, in the 5-day forecast, the reduced ensemble spread is more prevalent at the half circle toward the Pacific side (i.e., 90°E–180°–90°W; the right panel of Fig. 3b). These results inform us the preferred propagation of the reduced forecast error by the extra radiosonde observations. Coexistence of both reduced and increased forecast errors implies that the benefit of extra observations in one location is not ubiquitous, but limited in a space. Though the spread of the adverse impact is serious in the operational forecast perspective, the positive effect is worth being evaluated at least in our experimental forecasts with a research perspective. With this point in mind, we pay attention to Alaska, which is among the regions with the positive impact of extra observations and the significantly

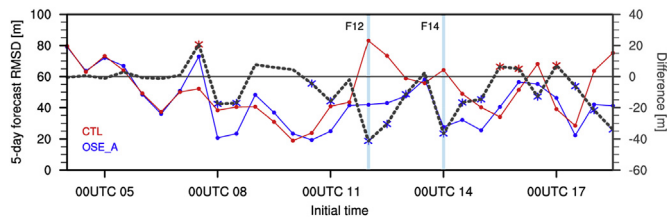


Fig. 4. The root mean square distances (RMSDs) of CTL_f (red line) and OSE_{A_f} (blue line) from ERA-I for H500, at forecast day 5, averaged over the Alaska domain, with the difference of the RMSDs (dotted line; OSE_{A_f} minus CTL_f). The asterisks denote the statistically significant differences ($p < 0.05$) based on bootstrap resampling. F12 and F14 refer to the forecast experiments with initial conditions of 00:00 UTC 12 August and 00:00 UTC 14 August, respectively, which show the largest improvement in OSE_{A_f} . (For interpretation of the references to color in this figure legend, the reader is referred to the Web version of this article.)

inhabited State of America.

Focusing on Alaska (60° – 70° N, 140° – 165° W), the evolutions of the area-mean ensemble-mean forecast errors of the 5-day forecast are compared for the 30 forecast experiments of CTL_f and OSE_{A_f} by calculating RMSDs from ERA-I (Fig. 4). Here the RMSD is defined by $\sqrt{1/N \sum_i \Delta_i^2}$, where N is the number of grids in the Alaskan box domain, Δ_i denotes the forecast increment at i th grid (i.e., the difference between CTL_f (or OSE_{A_f}) and ERA-I) and $\bar{(\)}$ expresses the ensemble-mean. In the forecasts with the earlier initial conditions (4–7 August), forecast performance is not much distinguishable between the two forecast sets. During this earlier spin-up period, the effect of additional data assimilation appears not to spread southeastward enough to influence the downstream Alaska domain. However, there exists an overall tendency towards the better performance of OSE_{A_f} after 8 August potentially due to the accumulating impact of the extra sounding data assimilation. The reduction of the 5-day forecast errors is found for 15 OSE_{A_f} forecast experiments among the total of 23 after 12:00 UTC 7 August. Among them, 14 OSE_{A_f} forecasts show statistically significant improvement ($p < 0.05$) by bootstrap resampling. In particular, two forecast experiments with initial conditions of 00:00 UTC 12 August (F12) and 00:00 UTC 14 August (F14) show the largest improvement in OSE_{A_f} . In the following section, the two outperformed forecast cases are examined in detail.

3.2. Selected outperformed forecasts

For the two outperformed forecasts (referred to as F12 and F14), the forecast time evolutions of area-mean H500 over Alaska are compared between CTL_f and OSE_{A_f} (Fig. 5). The better performance in OSE_{A_f} begins to appear after 3.5 days (i.e., 12:00 UTC 15 August) in the F12 case and after 2.5 days (i.e., 12:00 UTC 16 August) in the F14 case, respectively. As a result, the OSE_{A_f} shows outperformance of the 5-day forecast. The two forecast cases show the similar timing of the widening of the gap of the forecast performance (i.e., on 16 August), indicating that the improvement in OSE_{A_f} is related to the better simulation of the same synoptic weather phenomenon. As displayed later in Figs. 7 and 9, this synoptic weather phenomenon is a low pressure system migrating from the Bering Sea to Alaska.

How does the delayed widening of the gap of the forecast performance occur? Are they related to error propagations from upstream regions where the extra radiosonde observations have a substantial impact? To answer these questions, the spatiotemporal evolutions of the forecast errors against ERA-I are investigated from the initial time to forecast day 5 (120-h later). As for the F12 case, Fig. 6 displays the upper-level fields such as the T500 and the H500, while the low-level fields such as the PT850 and the MSLP are presented in Fig. 7. The both figures contain ERA-I as a reference, (left), the evolutions of the errors in CTL_f against ERA-I (middle), and the relative errors in OSE_{A_f} compared

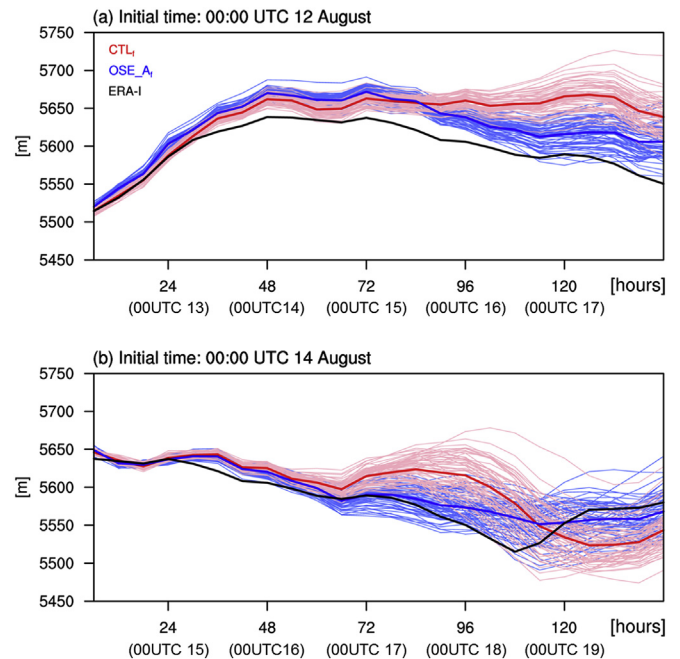
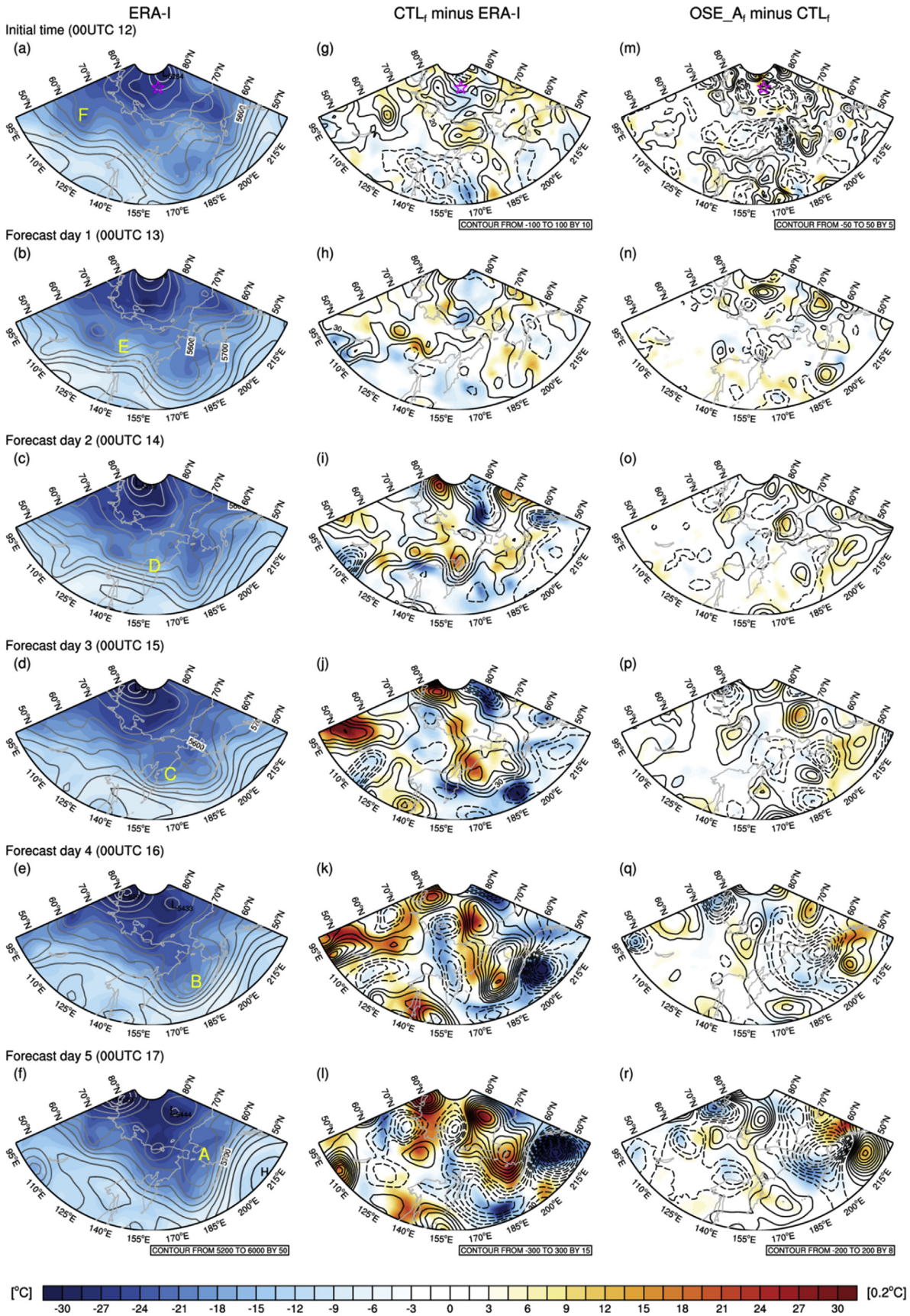


Fig. 5. The forecast time evolutions of area-mean H500 over Alaska for (a) F12 and (b) F14: individual ensemble members (thin line) and ensemble-mean (thick line) of CTL_f (red) and OSE_{A_f} (blue). The ERA-I (black thick line) reanalysis is presented as a reference value. (For interpretation of the references to color in this figure legend, the reader is referred to the Web version of this article.)

with CTL_f (right).

During the forecast days of F12 from 00:00 UTC 12 August, the overall synoptic meteorological features are the development of the upper-level trough–low-level low system over the Bering Sea while the pre-existing ridge is migrating toward Alaska (Fig. 6a–f, 7a–f). The ridge over Alaska is gradually replaced by the low pressure system from 16 August. The time series of area-mean H500 over Alaska well represents this synoptic evolution feature (Fig. 5a). As shown in Fig. 5a, the forecast errors of CTL_f over Alaska arise from the mispredicted height depression from forecast day 3.5 (12:00 UTC 15 August). To display the evolution of forecast errors, the error cores are picked up based on the H500 maps of analysis (Fig. 6g) and forecast errors (Fig. 6h–l) of CTL_f . Because the evolving error centers either split or merge over time, we manually track the error backward in time (Magnusson, 2017) at 6-hr intervals from the center of the maximum positive height errors over Alaska at forecast day 5 to determine source regions and propagation speeds of the errors contributing to the Alaska 5-day forecast. The resulting back-tracked centers are marked at 24-hr intervals with yellow alphabets (A, B, C, D, E and F) over the ERA-I maps (Fig. 6a–f). The error evolution maps of CTL_f (Fig. 6g–l; CTL_f minus ERA-I) demonstrate that the initial errors over Siberia, Russia (F) in the reanalysis develop into larger forecast errors in a few days and eventually affect the 5-day forecast performance over Alaska (E→D→C→B→A).

It is well known that the errors propagate with the group velocity of midlatitude baroclinic Rossby waves (Kelly et al., 2007). The propagating errors grow intrinsically with forecast time steps along the trough over the Bering Sea, resulting in a forecast bust over the downstream Alaska region. By contrast, the spatial pattern of the relative errors (i.e., OSE_{A_f} minus CTL_f) confirms the reduced analysis error in OSE_{A_f} (Figs. 6m and 7m) near the observation location and the increasing error reductions in OSE_{A_f} as the forecast progresses (Fig. 6n–r, 7n–r; i.e., the opposite pattern, compared with CTL_f minus ERA-I). The trivial-looking error reduction in the upstream region during the early forecast stage eventually amplifies and propagates eastward in the following days, leading to the improvement of the 5-



(caption on next page)

Fig. 6. Air temperature (shading) and geopotential height (contour) at 500 hPa from the initial time to forecast day 5 for the F12 case: (a–f) ERA-I, (g–l) CTL_f minus ERA-I, and (m–r) OSE_{A_f} minus CTL_f. The alphabet symbols in (a–f) indicate the back-tracked centers contributing to the positive height errors over Alaska at forecast day 5 which is detected from the difference fields of CTL_f minus ERA-I (g–l). Note the differing shading and contour intervals at the initial time for the difference fields (g, m). At the top panels, the location of the R/V *Araon* at the initial time is depicted by a pink star. The plot of difference uses rescaled units at the right side of the color bar. (For interpretation of the references to color in this figure legend, the reader is referred to the Web version of this article.)

day forecast in the downstream Alaska region (Figs. 6r and 7r).

As in Figs. 6 and 7, the same forecast fields are displayed for the other case of the large forecast error reduction (F14) (Figs. 8 and 9). Because the forecast initial time is two days late, the period from the initial time to forecast day 3 overlaps with that from forecast day 2–5 in F12. As in Fig. 6, the error cores (yellow alphabets: A, B, C, D1–D3, E1–E3 and F1–F3) are displayed over the ERA-I maps (Fig. 8a–f), which were also picked up by manual tracking (Magnusson, 2017) based on the H500 maps of analysis (Fig. 8g) and forecast errors (Fig. 8h–l) of CTL_f. Different from the F12 case, the three trajectories of forecast errors, which contributed to the large errors over Alaska at forecast day 5 for the F14 case, have been identified from the initial time to forecast day 3. The error evolution maps show that the three potential cores of initial analysis errors—one near the *Araon* radiosonde observations (F1), another over northeastern Russia (F2), and the other between them (F3) (Fig. 8g)—propagate eastward and merge into larger forecast errors over the migratory upper-level trough–low-level low system across the Bering Sea, which eventually affect the 3- to 5-day forecasts over the downstream Alaska region (Fig. 8h–l). In contrast to the F12 case, the low-level error propagation in the early forecast days is not clear for the F14 case (Fig. 9h and i), while it appears in the later days (Fig. 9j–l). The different forecast evolutions of the trough–low system, which were central to the large forecast error reduction over Alaska in OSE_{A_f} of F12, are also the source of the improvement in OSE_{A_f} of F14 (Fig. 8p–r, 9p–r). The spatial pattern of the relative errors of OSE_{A_f} compared with CTL_f (i.e., OSE_{A_f} minus CTL_f) evolves into an offset to the errors of CTL_f with increasing forecast steps, except over central northern Russia where a blocking pattern develops at forecast day 4 (Fig. 8e and f).

As shown above, for the F12 and F14 cases, the synoptic feature central to the large positive height errors of CTL_f over Alaska is the migratory upper-level trough–low-level low system crossing the Bering Sea. To contrast the different evolution of the system, we show the time–height evolutions of upper-level (200–500 hPa) PV along the relevant maximum cores of positive height errors in each day (Fig. 10). Here the manually back-tracked centers are displayed again (Fig. 10a and b) with alphabets as in Fig. 6a–f and 8a–f. The upper-level PV distribution along the routes of error evolution contrasts the error-originated differing evolutions of the upper-level dynamical flow between CTL_f and OSE_{A_f}, as compared with ERA-I. Both the forecast PV fields has a common low bias compared with ERA-I, but the bias is reduced in OSE_{A_f} (Fig. 10b–c, f–g). The F12 case has a single route originating from Siberia, Russia. Along the route, an offset signal to the low PV of CTL_f appears to propagate eastward, which increases the forecast PV at upper-levels toward the value of ERA-I (Fig. 10d). On the other hand, the forecast PV at upper-levels shows a large increase from point C (forecast day 3) for the F14 case (Fig. 10h). In fact, the sharp PV increase at point B on 18 August shown in ERA-I is not predicted by CTL_f of F14 (Fig. 10f), while it is captured by corresponding OSE_{A_f} (Fig. 10g). This reflects that the trough–low system in CTL_f migrates much slower to the Alaska region, which is related to the erroneous height evolution over Alaska (Fig. 5b).

4. Summary and discussion

In August 2015, upper-air sounding observations were regularly carried out around the Chukchi Sea during the Arctic research expedition of the Korean R/V *Araon*. With these special ship-borne vertical profile observations over the data-sparse open sea, we have

investigated whether the extra data assimilation of them into the ensemble forecast system could have a positive impact on the short-range predictability over Alaska, the nearest downstream-side inhabited land area from the observational area.

The results from the ensemble forecast experiments with 30 initial conditions of 12-hourly from 00:00 UTC 4 August to 12:00 UTC 18 August showed that the forecasts from the reanalysis data with extra radiosonde assimilations have an improved 5-day forecast skill in 15 forecasts among the total of 23 initial conditions after 3.5 days (i.e., 12:00 UTC 7 August). The delayed occurrence of the forecast improvement after several cycles of data assimilation implies the necessity of the accumulation of extra observations to have a widespread impact on the correction of background fields in previous analysis cycles.

Our experimental forecast study by focusing on Alaska showed that the radiosonde sounding observations around the Chukchi Sea improved the prediction of atmospheric flows. Considering the spatial distribution of absolute errors and ensemble spreads, however, the overall forecast improvement is found to be region-dependent (Figs. 2 and 3), which indicates the flow-dependent error evolution.

The presence of regions with a larger forecast error indicates that we should be careful to add spatially limited observations to analysis fields produced by operational forecast centers. In spite of the well-localized analysis increment of the ALEDAS2 around the observational area, an indispensable adverse impact on the flow should occur due to spinup effects of the dynamic adjustment to the analysis increment. Therefore, in the operational forecast perspective, wider spatial coverage of observations are necessary for a data-sparse region to lessen the adverse impact. Besides, the undesirable model response can be removed either by improving the data assimilation technique or by using different data assimilation technique such as the IAU process which gradually incorporates the analysis increments into a model integration (Bloom et al., 1996).

After analyzing the vertical structures of mid-latitude analysis and forecast errors in an ensemble of operational analyses, Hakim (2005) determined that forecast errors originate from analysis errors in the upper troposphere. In this respect, radiosonde sounding observations of the upper troposphere over the data-sparse Arctic Ocean effectively reduce initial analysis errors, resulting in suppression of the forecast error growth. This idea has been confirmed by several studies (Inoue et al., 2013, 2015; Sato et al., 2017; Yamazaki et al., 2015).

The YOPP is underway during 2017–19 (Jung et al., 2016). During the YOPP period, more real-time observations in the polar atmosphere are available to the operational forecast centers over the globe. The leading forecast center such as the ECMWF will evaluate the additional polar observation impacts on weather and climate predictions in an operational forecast perspective. Thereafter, it is expected to promote international efforts on the sustainable polar observing network.

Acknowledgements

M.-H.L. and J.-H.K. were funded by the KPOPS (KOPRI, PE18130) project and J.-H.K. was also funded by the K-AOOS (KOPRI, 20160245, funded by the MOF, Korea) project. J.I., K.S., and A.Y. were supported by the ArCS Project. J. I. was also supported by a Grant-in-Aid for Scientific Research (KAKENHI 18H03745, 18KK0292). K. S. was also supported by KOPRI Asian Polar Science Fellowship Program. ALEDAS2 and AFES integrations were performed on the Earth Simulator with the support of JAMSTEC. This is a contribution to the Year of Polar Prediction (YOPP), a flagship activity of the Polar Prediction Project

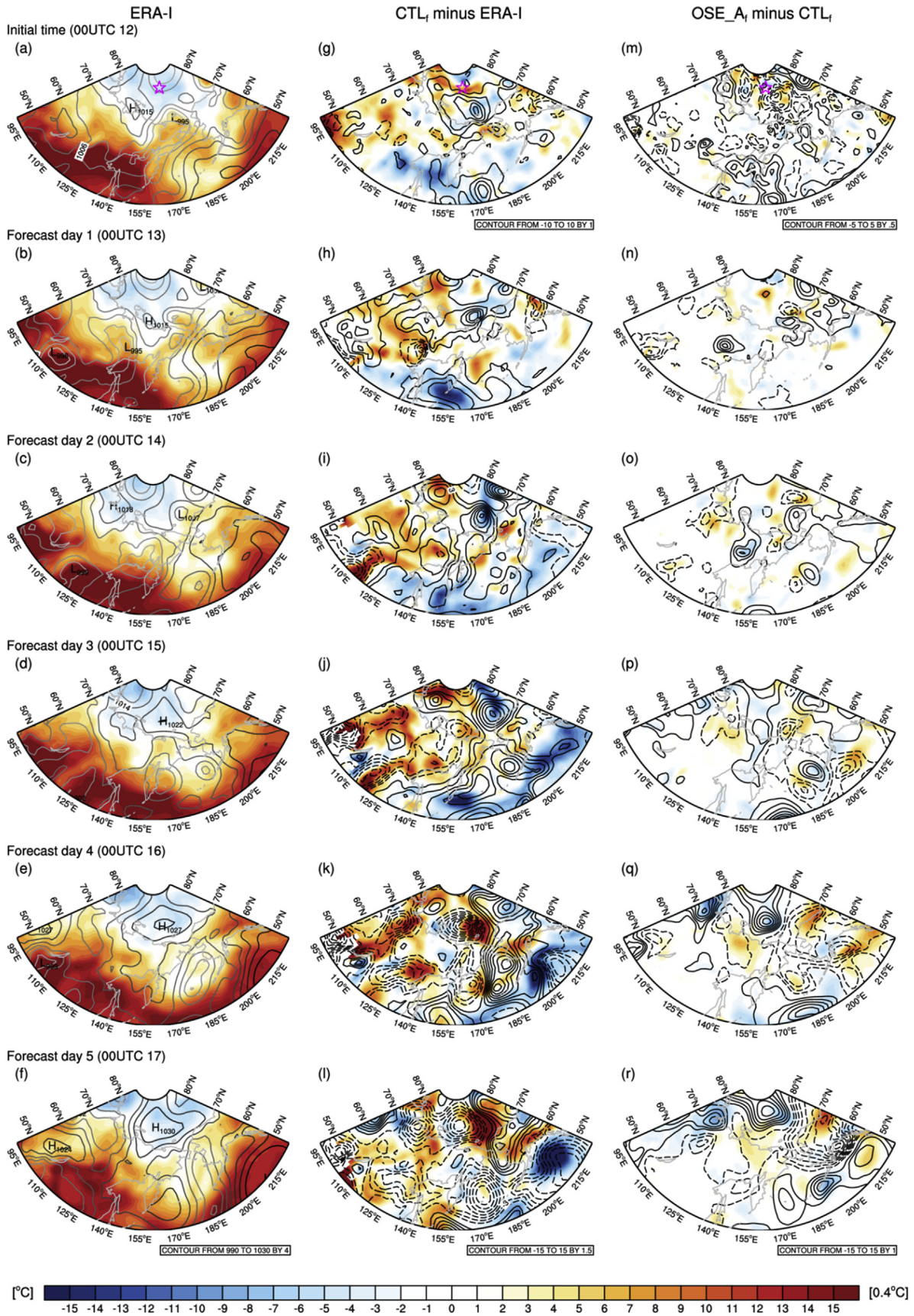


Fig. 7. Same as Fig. 6, except for potential temperature at 850 hPa (shading) and mean sea level pressure (contour).

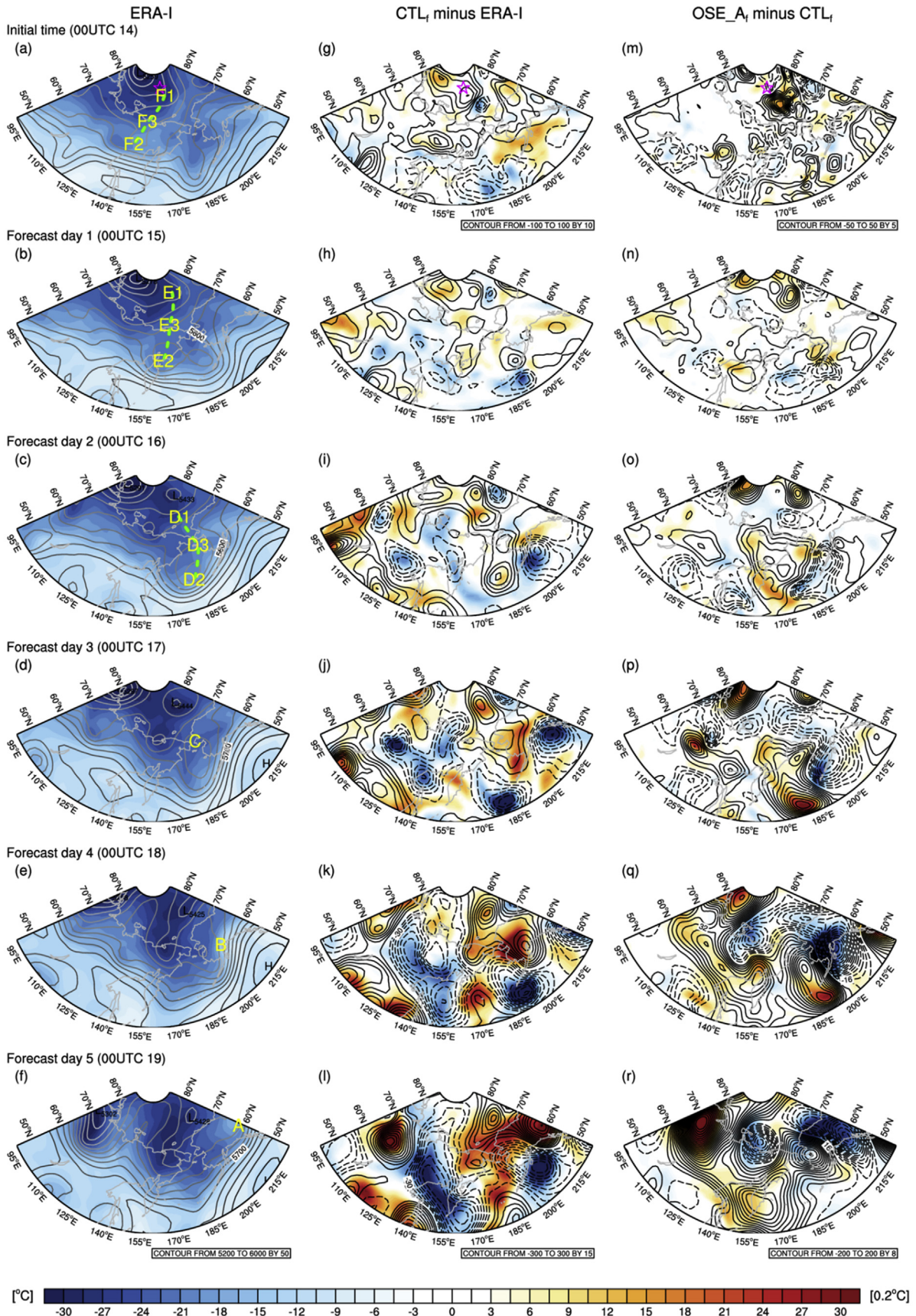


Fig. 8. Same as Fig. 6, except for the F14 case.

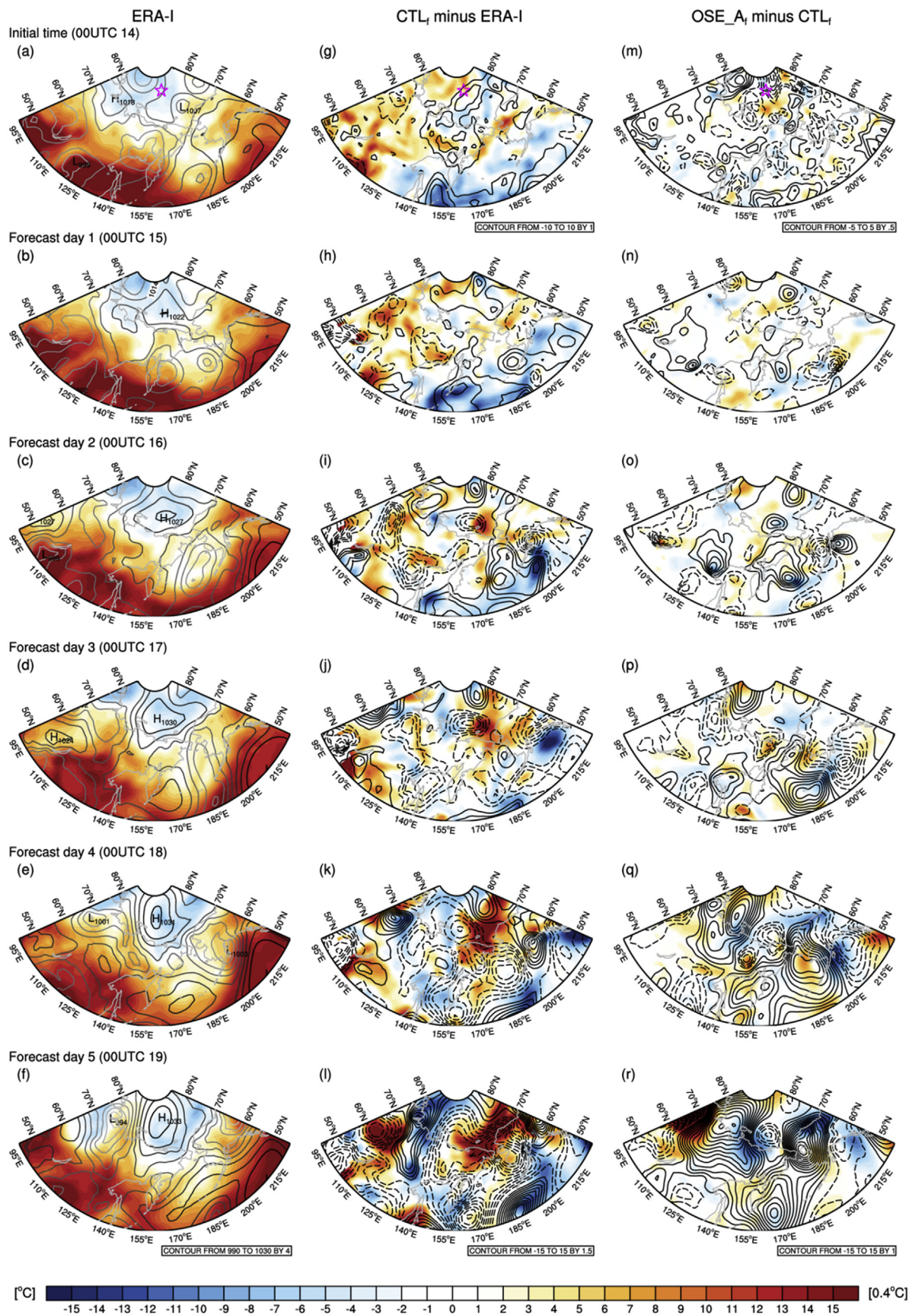


Fig. 9. Same as Fig. 7, except for the F14 case.

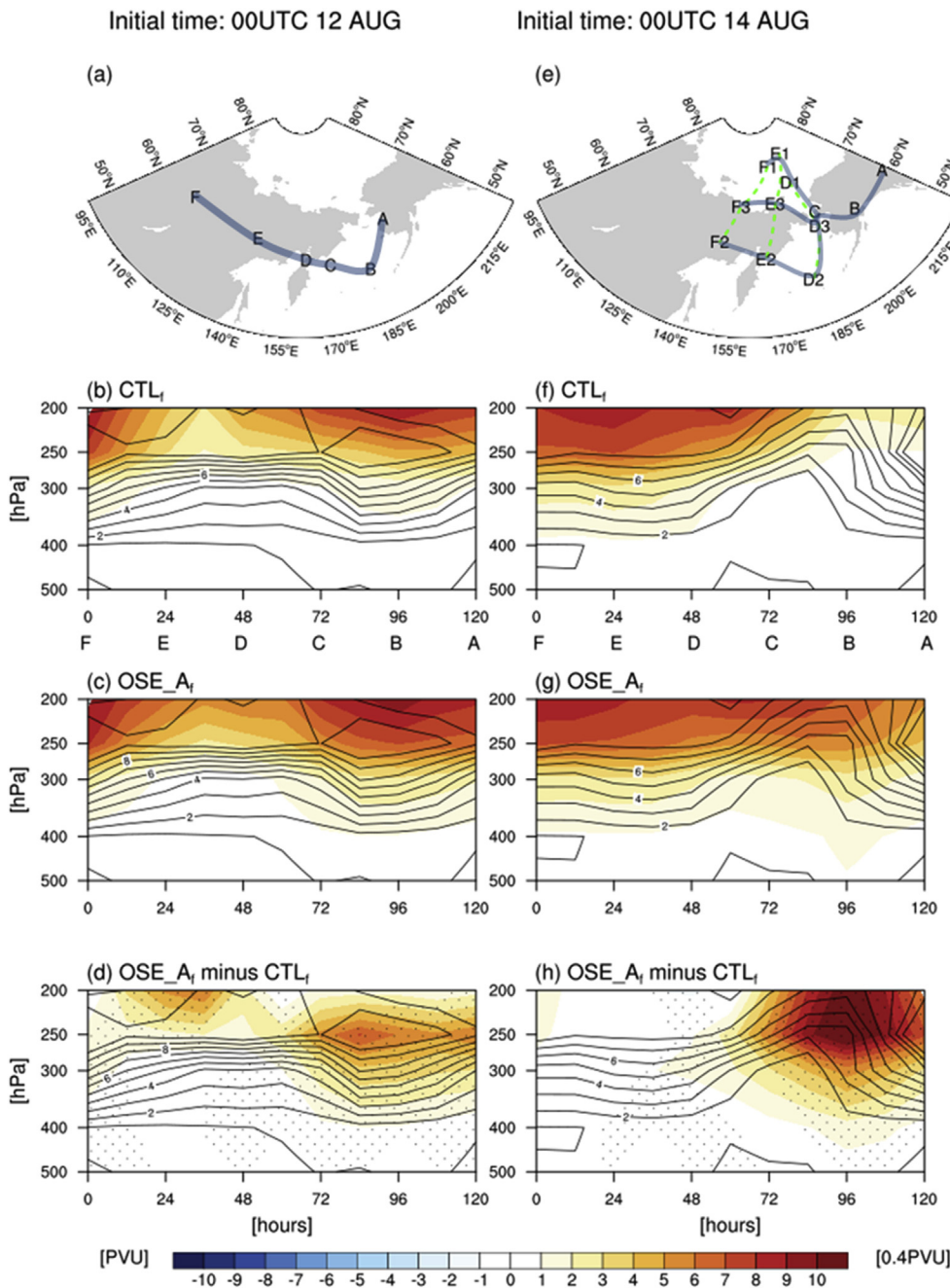


Fig. 10. The propagation routes of the errors manually tracked backward from North America at forecast day 5 (mark ‘A’) for (a) the F12 case and (e) the F14 case, where the daily centers are marked with alphabets as in Figs. 6 and 8. For the F14 case, three routes are detected contributing to the positive height error over the western coast of Alaska at forecast day 3 (mark ‘C’). For the F12 case, the vertical cross sections of upper-level total PV along the routes of error evolution are displayed in (b) for CTL_f and in (c) for OSE_{A_f} . Their difference field (i.e., OSE_{A_f} minus CTL_f) is placed in (d). Corresponding plots for the F14 case are shown in (f) for CTL_f , in (g) for OSE_{A_f} and in (h) for OSE_{A_f} minus CTL_f , where the average PV fields over the three routes are used. For a comparison, the corresponding PV fields from the ERA-I (contour) are overlaid in all vertical cross section plots. In (d) and (h), the dots represent the points where the difference is statistically significant ($p < 0.05$) based on bootstrap resampling.

(PPP), initiated by the World Weather Research Programme (WWRP) of the World Meteorological Organization (WMO).

References

Bloom, S.C., Takacs, L.L., Silva, A.M., Ledvina, D., 1996. Data assimilation using incremental analysis updates. *Mon. Wea. Rev.* 124, 1256–1271.
 Cohen, J., Ye, H., Jones, J., 2014. Recent arctic amplification and extreme mid-latitude weather. *Nat. Geosci.* 17, 627–637.
 Coumou, D., Lehmann, J., Beckmann, J., 2015. The weakening summer circulation in the Northern Hemisphere mid-latitudes. *Science* 348, 324–326.
 Dee, D.P., et al., 2011. The ERA-Interim reanalysis: configuration and performance of the data assimilation system. *Q. J. R. Meteorol. Soc.* 137, 553–597.
 Enomoto, T., Miyoshi, T., Moteki, Q., Inoue, J., Hattori, M., Kuwano-Yoshida, A., Komori, N., Yamane, S., 2013. Observing-system research and ensemble data assimilation at JAMSTEC. In: Park, S.K., Xu, L. (Eds.), *Data Assimilation for Atmospheric, Oceanic and Hydrologic Applications*. Springer, Berlin, pp. 509–526.
 Hakim, G.J., 2005. Vertical structure of midlatitude analysis and forecast errors. *Mon. Weather Rev.* 133, 567–578.
 Hesterberg, T., Moore, D.S., Monaghan, S., Clipson, A., Epstein, R., 2003. Bootstrap

methods and permutation tests. In: Moore, D.S., McCabe, G.P. (Eds.), *Introduction to the Practice of Statistics*. W. H. Freeman & Co., New York, pp. 14.1–14.70.
 Inoue, J., Enomoto, T., Hori, M.E., 2013. The impact of radiosonde data over the ice-free Arctic Ocean on the atmospheric circulation in the Northern Hemisphere. *Geophys. Res. Lett.* 40, 864–869. <https://doi.org/10.1002/grl.50207>.
 Inoue, J., Yamazaki, A., Ono, J., Dethloff, K., Maturilli, M., Neuber, R., Edwards, P., Yamaguchi, H., 2015. Additional Arctic observations improve weather and sea-ice forecasts for the Northern Sea Route. *Sci. Rep.* 5, 16868. <https://doi.org/10.1038/srep16868>.
 Jung, T., et al., 2016. Advancing polar prediction capabilities on daily to seasonal time scales. *Bull. Am. Meteorol. Soc.* 97, 1631–1647.
 Kelly, G., Thepaut, J.-N., Buizza, R., Cardinali, C., 2007. The value of observations. I: data denial experiments for the Atlantic and the Pacific. *Q. J. R. Meteorol. Soc.* 133, 1803–1815.
 Kim, B.-M., Son, S.-W., Min, S.-K., Jeong, J.-H., Kim, S.-J., Zhang, X., Shim, T., Yoon, J.-H., 2014. Weakening of the stratospheric polar vortex by Arctic sea-ice loss. *Nat. Commun.* 5, 4646. <https://doi.org/10.1038/ncomms5646>.
 Magnusson, L., 2017. Diagnostic methods for understanding the origin of forecast error. *Q. J. R. Meteorol. Soc.* 143, 2129–2142.
 Miyoshi, T., Yamane, S., 2014. Local ensemble transform Kalman filtering with an AGCM at a T159/L48 resolution. *Mon. Weather Rev.* 135, 3841–3861.

- Mori, M., Watanabe, M., Shiogama, H., Inoue, J., Kimoto, M., 2014. Robust arctic sea-ice influence on the frequent Eurasian cold winters in past decades. *Nat. Geosci.* 7, 869–873. <https://doi.org/10.1038/ngeo2277>.
- Ohfuchi, W., Nakamura, H., Yoshioka, M.K., Enomoto, T., Takaya, K., Peng, X., Yamane, S., Nishimura, T., Kurihara, Y., Ninomiya, K., 2004. 10-km mesh meso-scale resolving simulations of the global atmosphere on the Earth Simulator – preliminary outcomes of AFES (AGCM for the Earth Simulator) –. *J. Earth Simulator* 1, 8–34.
- Ono, J., Inoue, J., Yamazaki, A., Dethloff, K., Yamaguchi, H., 2016. The impact of radiosonde data on forecasting sea-ice distribution along the Northern Sea Route during an extremely developed cyclone. *J. Adv. Model. Earth Syst.* 8, 292–303. <https://doi.org/10.1002/2015MS000552>.
- Overland, J., Dethloff, K., Francis, J., Hall, R., Hanna, E., Kim, S.-J., Screen, J., Shepherd, T., Vihma, T., 2016. Nonlinear response of mid-latitude weather to the changing Arctic. *Nat. Clim. Change* 6, 992–999. <https://doi.org/10.1038/nclimate3121>.
- Sato, K., Inoue, J., Yamazaki, A., Kim, J.-H., Maturilli, M., Dethloff, K., Hudson, S.R., Granskog, M.A., 2017. Improved forecasts of winter weather extremes over mid-latitudes with extra Arctic observations. *J. Geophys. Res. Oceans* 122. <https://doi.org/10.1002/2016JC012197>.
- Yamazaki, A., Inoue, J., Dethloff, K., Maturilli, M., König-Langlo, G., 2015. Impact of radiosonde observations on forecasting summertime Arctic cyclone formation. *J. Geophys. Res.* 120, 3249–3273.